Agricultural and Forest Meteorology 341 (2023) 109635

Contents lists available at ScienceDirect

Agricultural and Forest Meteorology

journal homepage: www.elsevier.com/locate/agrformet

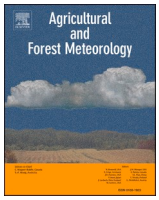

Comparing forest and grassland drought responses inferred from eddy covariance and Earth observation

Anne J. Hoek van Dijke [a,b,c,d,*], René Orth [a], Adriaan J. Teuling [d], Martin Herold [c,e], Martin Schlerf [b], Mirco Migliavacca [f], Miriam Machwitz [b], Theresa C. van Hateren [b,d], Xin Yu [a,g], Kaniska Mallick [b,h,*]

[a] Department of Biogeochemical Integration (BGI), Max Planck Institute for Biogeochemistry, Jena 07745, Germany
[b] Remote Sensing and Natural Resources Modelling Group, ERIN Department, Luxembourg Institute of Science and Technology (LIST), Belvaux, Luxembourg
[c] Laboratory of Geo-Information Science and Remote Sensing, Wageningen University and Research, Wageningen, the Netherlands
[d] Hydrology and Quantitative Water Management Group, Wageningen University and Research, Wageningen, the Netherlands
[e] Remote Sensing and Geoinformatics, Telegrafenberg, Helmholtz GFZ German Research Centre for Geosciences, Potsdam, Germany
[f] Joint Research Centre, European Commission, Ispra, (VA) 21027, Italy
[g] Department of Ecology, University of Innsbruck, Innsbruck 6020, Austria
[h] Biometeorology Lab, Environmental Science Policy and Management, University of California, Berkeley, CA, United States

ARTICLE INFO

Keywords:
Remote sensing of vegetation
Eddy covariance data
Surface conductance
Vegetation drought response
Water energy and carbon fluxes

ABSTRACT

Temperate forests and grasslands have different drought response strategies. Trees often control their stomatal opening to reduce water loss to prevent hydraulic failure and ensure the sustainable above-ground biomass production. In contrast, grasses generally have a less strong stomatal control and maintain high photosynthesis and transpiration until the soil moisture gets depleted. That is when their leaves wilt and the grasslands reduce their aboveground green biomass. Both the increased stomatal control and the reduction in aboveground biomass decrease the canopy-surface conductance and decrease the exchange of water and carbon between the leaves and the atmosphere. Here, we study to which extent remote sensing data reflect the drought-induced reduction in canopy-surface conductance for forests and grasslands. We use eddy covariance observations over 63 sites across the northern hemisphere to infer the conductance. We identify severe droughts from low soil moisture content and reduced canopy-surface conductance. We further analysed how the drought response is reflected in thermal and optical data derived from MODIS satellite data. The results show that the land surface temperature increases with drought-induced reductions in canopy-surface conductance for both forests and grasslands. By contrast, the optical indices (e.g., the normalized difference vegetation index) show a much stronger response for grasslands as compared to the forests. We conclude that the different canopy-level drought response strategies of trees and grasses are widespread and that these different responses are reflected in remote sensing data. Hence, a combination of thermal and optical satellite data should be used to monitor and study vegetation drought responses of forests and grasslands to ensure accurate inference on the implications on water, energy, and carbon fluxes.

1. Introduction

During a drought, low soil moisture availability in the root zone in conjunction with a high atmospheric evaporative demand triggers vegetation reactions (Fu et al., 2022; Lansu et al., 2020). The first vegetation response to drought is a strong stomatal regulation to increase the water use efficiency and reduce root-zone water loss (Peters et al., 2018). Prolonged soil moisture drought can induce changes in the vegetation state, such as a decrease in the leaf pigments, the leaf water content, and leaf turgor and structure (Salehi-Lisar and Bakhshayeshan-Agdam, 2016). When the drought conditions persist even longer, this can result in the defoliation of the vegetation and mortality (Brodribb et al., 2020; Choat et al., 2018; Senf et al., 2020). While the strong stomatal regulation is a rapid and reversible response, the effects on the vegetation structure can sometimes be irreversible. Both, the stomatal regulation and a change in green leaf area, impact the surface

* Corresponding authors at: Remote Sensing and Natural Resources Modelling Group, ERIN Department, Luxembourg Institute of Science and Technology (LIST), Belvaux, Luxembourg.
E-mail addresses: annehvd@bgc-jena.mpg.de (A.J. Hoek van Dijke), kaniska.mallick@list.lu (K. Mallick).

https://doi.org/10.1016/j.agrformet.2023.109635
Received 24 December 2022; Received in revised form 26 June 2023; Accepted 30 July 2023
Available online 7 August 2023

conductance (G_s, the aggregated stomatal conductance of the entire canopy), and simultaneously affects the exchange of water and carbon between the leaves and the atmosphere. The exact vegetation response to drought and the impacts on the water, energy, and carbon balance, depends on the timing, intensity, and duration of the drought, as well as the species type and climate (Krasnova et al., 2022; O et al., 2022; Obladen et al., 2021; Pranindita et al., 2021; van Hateren et al., 2021).

In temperate climates, grasslands and forests respond differently to drought because of their different drought response strategies (Fig. 1), (Zhang et al., 2016). Grasslands take the risk to lose their aboveground biomass, while they survive belowground (Zha et al., 2010). Trees cannot take this risk and therefore have to adopt a more conservative water-use behavior in order to survive moderate droughts. As a result, trees adopt a stronger stomatal regulation and increase their water use efficiency to decrease water loss, while grasslands generally prioritize high evaporation (Whitehead, 1998; Wolf et al., 2013). When grassland soil moisture gets depleted, their leaves wilt. This reduction in the aboveground biomass is directly reflected in the grassland's appearance. However, due to the conservative behavior of trees, drought is not always directly reflected in the forests' appearance (Mallick et al., 2016), but, the effects are sometimes visible in the following year's growth and leaf area (Anderegg et al., 2015; Kannenberg et al., 2019; Schuldt et al., 2020; Senf and Seidl, 2021). Through these different drought coping strategies, grasslands and forests have a different impact on evaporation, precipitation, heat waves, and carbon exchange during droughts (Graf et al., 2020; Pranindita et al., 2021; Teuling et al., 2010; Vicca et al., 2016). A better understanding of the different drought coping strategies and the monitoring of the vegetation drought response can improve future drought monitoring as well as the development of process-based models.

The surface conductance G_s is a one of the key ecophysiological variables in the land-atmosphere exchange of water, energy, and carbon. Drought-induced reductions in G_s decrease the exchange of water and carbon, and thereby impact local and regional weather and climate. For example, the reduction in evaporation decreases the evaporative cooling and increases the intensity of heat waves that often coincide with drought (Miralles et al., 2019; O et al., 2022). Furthermore, the reduction in evaporation reduces the moisture recycling and increases the drought risk downwind (Herrera-Estrada et al., 2019; Miralles et al., 2019; Pranindita et al., 2021; Schumacher et al., 2019). Additionally, the reduction in carbon uptake significantly reduces the terrestrial carbon sink, and droughts can even switch forests from a carbon sink into a source of carbon (Ciais et al., 2005; Granier et al., 2007; Haberstroh et al., 2022; Mekonnen et al., 2017). Because of these major impacts of droughts on weather and climate, it is important to understand and monitor the drought-induced changes in G_s. Recent studies to the stomatal or surface conductance indicate that they vary with vegetation type and climate (De Kauwe et al., 2017; Lin et al., 2015); these studies have however not studied how the conductance changes during droughts. Several methods exist for large-scale monitoring of G_s, for example through parameterization of G_s from satellite-based land surface temperature and vegetation indices or by using satellite data to scale in-situ measurements over larger areas (Nemani and Running, 1989; Yebra et al., 2013). The representation of surface and stomatal conductance in land surface models has received major attention in the past years (De Kauwe et al., 2015; Franks et al., 2018; Oliver et al., 2022). A better understanding of the drought-induced reductions in surface conductance and a better monitoring strategy can contribute to further improvements of land-atmosphere fluxes in land surface models.

While the differences between the forest and grassland drought response strategies have been shown in site-scale studies (e.g. Teuling et al., 2010; Whitehead, 1998; Wolf et al., 2013; Zha et al., 2010), it is less clear if these contrasting mechanisms act at larger spatial scales and can be observed through satellite data. Therefore, we studied to which extent remote sensing data reflects the contrasting drought responses for forest and grassland. We focus on thermal infrared and optical remote sensing data which both play an important role in vegetation drought monitoring. Thermal infrared remote sensing (wavelength of 8 - 14 μm) is used to obtain the land surface temperature (LST) and is sensitive to evaporative cooling. Therefore, thermal data can be used to detect the changes in vegetation functioning and G_s when the vegetation's structure is not (yet) altered (Mallick et al., 2022; Mallick et al., 2018; Vicca et al., 2016). Also thermal infrared derived indices, such as LST minus air temperature (LST − Ta) and the Crop Water Stress Index (CWSI) were successfully used to monitor plant water stress (Ekinzog et al., 2022; Gerhards et al., 2019; Veysi et al., 2017). Optical remote sensing measures the reflection of solar radiation by the soil and the vegetation in the visible, near-infrared, and shortwave infrared wavelengths. The visible wavelengths (0.4 - 0.7 μm) can be used to detect, amongst others, changes in leaf chlorophyll content during vegetation browning. The near-infrared wavelengths (0.7 – 1.4 μm) can be used to detect changes in vegetation and cell structure. Shortwave infrared wavelengths (1.3 – 2.5 μm) are sensitive to the leaf water content and to the green leaf area. Vegetation indices derived from the visible and near-infrared

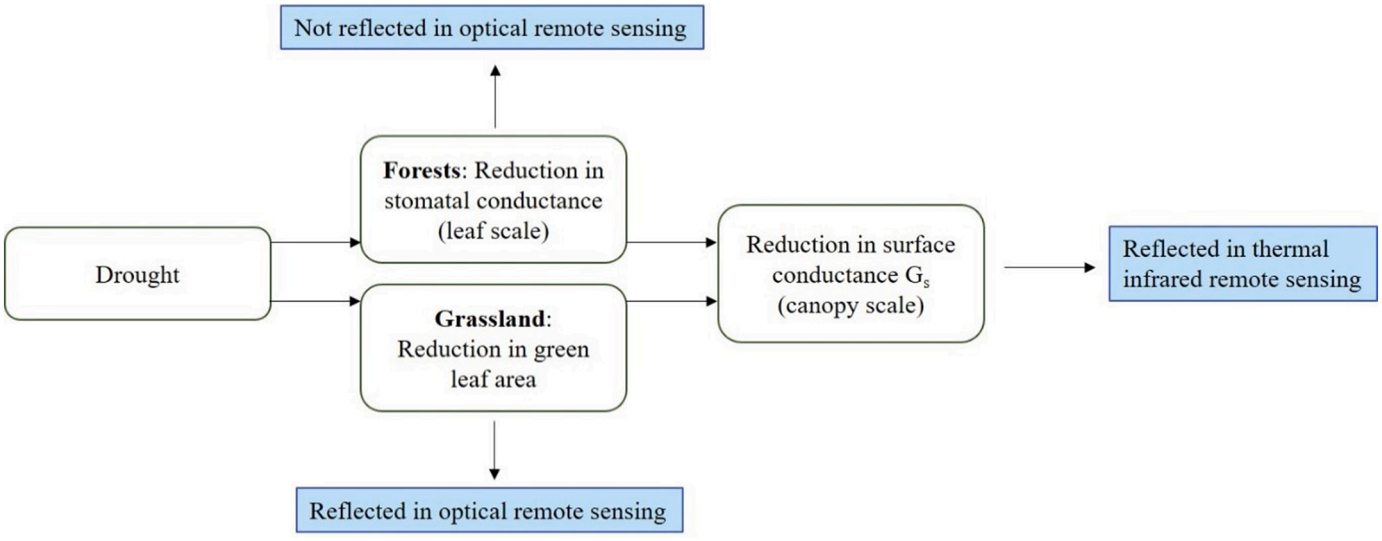

Fig. 1. Visual representation of the hypothesis of this study. We hypothesise that the contrasting drought response for forests and grasslands results in different remote sensing signals.

wavelengths have therefore been used extensively in drought detection (Bachmair et al., 2018; Buitink et al., 2020; Buras et al., 2020; Gerhards et al., 2016; van Hateren et al., 2021; Vicca et al., 2016). A few frequently used indices include the Normalized Difference Vegetation Index (NDVI), the Enhanced Vegetation Index (EVI), the Near-Infrared Reflectance of Vegetation (NIRv), and the Structural Insensitive Pigment Index (SIPI). Their performance to monitor vegetation droughts depends, among others, on the climate, drought intensity, and the vegetation type, but these optical indices have generally been found to perform better in short vegetation than forests (Quiring and Ganesh, 2010; Vicente-Serrano, 2007). Given the different drought response strategies of forests and grasslands, and the different properties of thermal infrared and optical remote sensing, we formulate the following hypothesis (Fig. 1):

> For forest, drought-induced changes in the surface conductance G_s are reflected in thermal infrared based data but not in optical based data, while for grassland, drought-induced changes in the surface conductance G_s are reflected in both thermal infrared and in optical based data.

2. Methods

In this study, the surface conductance G_s was calculated from eddy covariance site data. For drought years, years with unusual dry soil moisture conditions, the onset of the vegetation drought response was

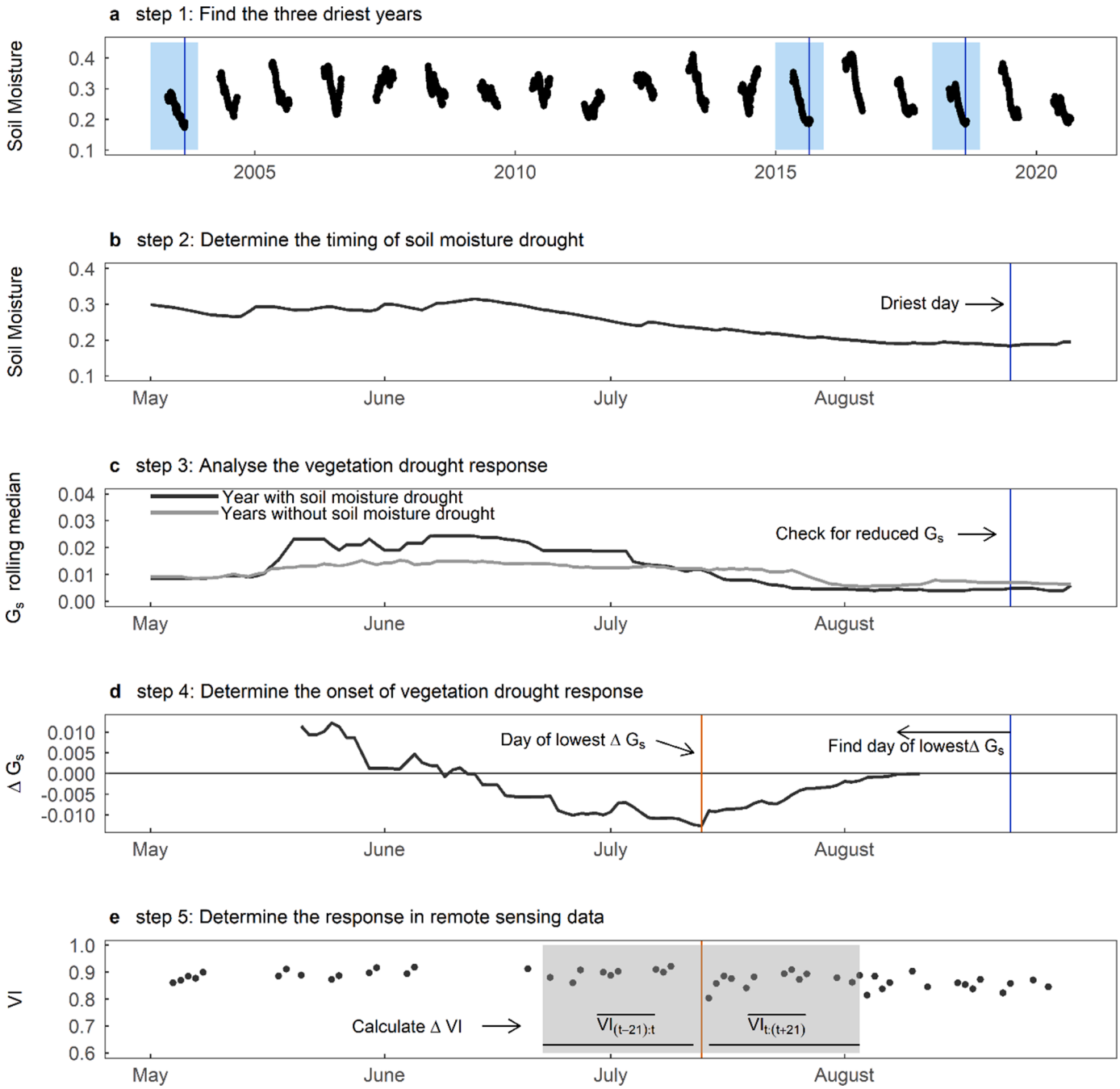

Fig. 2. Illustration of our methodology. In (a) step 1 and (b) step 2 we identify the soil moisture drought, in (c) step 3 and (d) step 4 we identify the vegetation drought response from in-situ observations, and in (e) step 5 we study the response in remote sensing data (the vegetation indices, VI) to the drought-induced reduction in the surface conductance (G_s). The details of each step are described in Section 2.4.

identified. The onset was defined as the moment of strongest reduction in G_s. Afterwards, MODIS satellite data were used to study how the reduction in G_s, detected from eddy covariance data, is reflected in remote sensing data. This was done by comparing the satellite data before and after the onset of vegetation drought response. This study includes 57 sites in the Northern Hemisphere and focusses on the summer months (May - August) of the years 2003 – 2020.

2.1. Study sites

Eddy covariance data were collected from four different sources: FLUXNET2015 (Pastorello et al., 2020), ICOS drought 2018 (Centre, 2020), ICOS Warm Winter 2020 (Warm Winter et al., 2022), and Ameriflux (https://ameriflux.lbl.gov/). These datasets are compatible and are produced using the ONEFlux processing codes (Pastorello et al., 2020). Within these datasets, all sites were selected that: [1] were situated in the Northern Hemisphere (179 sites), [2] had a grassland or forest land cover (113 sites), [3] had (half) hourly data available for sensible heat, latent heat, air temperature, air pressure, and friction velocity (102 sites), [4] had a vegetation drought response during the severe drought years (methods section 2.4, 64 sites. Note that 18 sites were excluded because they had no data available for drought years or no G_s data available for the driest day (Fig. 2), and another 20 sites were excluded because the vegetation drought response was not detected for the drought year(s)), and [5] had data available for at least one drought year and at least three reference years (methods section 2.4, 57 sites). The final data set used in this study contains 10 grassland sites and 47 forest sites (methods section 2.4, Supplementary).

2.2. Eddy covariance data and calculation of G_s

For every site, we use the half hourly (if not available: hourly), gap-filled, flux tower measurements of the latent heat flux (*LE*), sensible heat flux (*H*), gross primary productivity (GPP), friction velocity (u^*), air temperature (T_A), relative humidity (RH), air pressure (P_A), and incoming shortwave radiation (R_g). (Half) hourly data of *LE* and *H* were discarded in three cases: 1) if the fluxes had a quality label ́poor data ́or ́medium data ́, 2) in the 48 hours after rainfall, to minimise the effect of soil and interception evaporation, and 3) during the most stable atmospheric conditions (friction velocity $u^* < 0.1$ m s^{-1}). RH was used to calculate the actual vapor pressure, and R_g and T_A were used to calculate the partial correlation in section 3.3. *LE*, *H*, T_A, and P_A were used in the calculation of G_s. We performed the same analyses with the energy-balance corrected eddy covariance data, but this did not significantly change the detection of the onset of vegetation drought response.

The surface conductance was computed using the Flux-Gradient equations (Wehr and Saleska, 2021). These equations can be used to derive G_s from the vapor pressure difference across the canopy-integrated stomata and the evaporative flux. G_s is calculated according to Eq. (1):

$$G_s = \frac{1}{r_{sV}}, \tag{1}$$

where G_s is the surface conductance in m s^{-1}, which is the reciprocal of surface resistance (r_{sV}) [s m^{-1}]. r_{sV} is calculated according to Eq. (2):

$$r_{sV} = \frac{(e^*(T_L) - e)}{R * (T_A + 273.15) * E} - r_{av}, \tag{2}$$

where $e^*(T_L)$ is the saturated vapor pressure inside the leaf [Pa], and e is the actual vapor pressure of the air [Pa]. $e^*(T_L)$ is calculated according to Eq. (9) in Paw U and Gao (1988). R is the universal gas constant, T_A is the air temperature [°C], and E is the water vapor flux [mol m^{-2}s^{-1}]. r_{aV} is the aerodynamic resistance to water vapor [s m^{-1}]. The canopy integrated leaf temperature T_L is calculated using Eq. (3):

$$T_L = \frac{(H * r_{aH})}{\rho_A * C_p} + T_A, \tag{3}$$

where H is the sensible heat flux [W m^{-2}], and r_{aH} is the aerodynamic resistance to heat [s m^{-1}]. ρ_A is the density of wet air [kg m^{-3}], calculated as $\rho_A = \rho_{A,dry} + \rho_v$ [kg m^{-3}], where $\rho_{A,dry}$ is the density of dry air and ρ_v is the density of water vapor. c_p is the specific heat of air (1013 J kg^{-1}K^{-1}), and T_A is the air temperature [°C]. r_{aH} and r_{aV} are calculated according to Eqs. (4) and (5):

$$r_{aH} = r_{bH} + r_{am}, \tag{4}$$

$$r_{aV} = r_{bV} + r_{am}, \tag{5}$$

where r_{bV} and r_{bH} are the leaf boundary layer resistances to water vapor and heat, respectively [s m^{-1}], and r_{am} is the aerodynamic resistance for momentum [s m^{-1}] which is calculated from Eq. (6):

$$r_{am} = \frac{u}{u^{*2}}, \tag{6}$$

where u is the wind speed [m s^{-1}] and u^* is the friction velocity [m s^{-1}]. r_{bH} can be calculated using an empirical equation based on, among others, the leaf area index and characteristic leave dimension. In this study, the calculation was attempted, but not practical because of the uncertainty in, and sensitivity to, this length scale of the leaves. Furthermore we did not use the empirical equation based on satellite remote sensing data, to ensure an independent assessment of G_s with respect to the satellite derived drought indices. Instead we assume a constant value of 10 s m^{-1} (based on Wehr and Saleska (2021)) for all vegetation types. r_{bH} however varies with vegetation characteristics and wind speed, and can reach values higher than 10 s m^{-1}. To test the effect of this assumption, we also analysed the values $r_{bH} = 8$ and 20 s m^{-1}. These different values for r_{bH} did not change the results significantly and did not affect the conclusions of the study (Supplementary Fig. S1). r_{bV} is calculated following Eq. (7):

$$r_{bV} = \frac{1}{f} * r_{bH} * \left(\frac{Sc}{Pr}\right)^{\frac{2}{3}}, \tag{7}$$

where f is the mean stomatal ratio, Sc is the Schmidt number for water vapor ($Sc = 0.67$), and Pr is the Prandtl number for air ($Pr = 0.71$). f was set to 1, assuming all sites have amphistomatic leaves (having stomata on both sides of the leaves), because it was not possible to determine the mean stomatal ratio for each site.

Negative values of G_s were omitted. Daily mean G_s was calculated if at least 50% of the (half) hourly values were available. For the analyses, we gap-filled the G_s time series by calculating the 21-day rolling median G_s value.

2.3. Satellite data and calculation of the vegetation indices

Remote sensing data were available from the Version 6.1 MODIS products MOD09GA (Vermote and Wolfe, 2021b), MYD09GA (Vermote and Wolfe, 2021a), MOD11A1 (Wan et al., 2021b), and MYD11A1 (Wan et al., 2021a). These data are collected by the Terra (MOD) and Aqua (MYD) satellites. For both satellites the daytime observations were used (around 10:30 for Terra and 13:30 for Aqua). For each product, the quality label was used to remove the cloudy data. The data have a spatial resolution of 500 m (MOD and MYD09GA) and 1 km (MOD and MYD11A1).

For MODIS band 1 (NIR), 2 (Red), and 3 (Blue), mean daily values were calculated from both Terra and Aqua data, and either Terra or Aqua data were used when only one of them was available. For land surface temperature (LST), MODIS Aqua data were used, because the afternoon overpass time is better able to capture drought stress.

However, when Aqua data were not available, MODIS Terra data were used, which were first adjusted using a linear regression between the Aqua and Terra data. Afterwards, seven different optical and thermal infrared indices were calculated (Table 1). The results of the NDVI and LST are presented in the main text, and the other indices are presented in the supplementary information.

The 500 × 500 m and 1 × 1 km spatial resolution of the MODIS data was not always representative for the flux tower footprint. The size, location, and shape of flux tower footprints change continuously, driven by changes in surface roughness, wind direction and wind speed (Kong et al., 2022), while the same one MODIS pixel was used over time. Besides these dynamics over time, some sites have a mixed land cover in the satellite data, which is only partly representative for the flux tower land cover. Satellite products with a higher spatial resolution could however not be used because of their low temporal resolution (Landsat series) or limited time coverage and lack of thermal infrared bands (Sentinel-2).

2.4. Methodology

The methodology consisted of five steps: in step 1 and 2 the soil moisture droughts were identified based on reanalysis data, in step 3 and 4 the vegetation drought response was analysed based on in-situ observations, and in step 5 the remote sensing indices were used to study the drought response in satellite data (Fig. 2).

Step 1 Find the three driest years.

For every site, the three driest years were identified for the total study period of 2003 – 2020 (summer months only) (Fig. 2a). The driest years were the three years with the lowest minimum summer soil moisture content in the upper 1 m of the soil (weighted mean over ERA5-Land reanalysis soil moisture layer 1, 2, and 3) (Muñoz Sabater, 2019, accessed January 2020). We use the ERA5-Land soil moisture data as a generic and generally available indicator for soil moisture droughts. For most sites, the eddy covariance data did not span the full study period of 2003 – 2020. Therefore, sites were discarded when no eddy covariance data were available for the three driest years.

Step 2 Determine the timing of soil moisture drought.

For every of the three driest years from step 1, the day of the strongest soil moisture drought was determined (Fig. 2b). This was the day with the lowest soil moisture value.

Step 3 Analyse the vegetation drought response.

For each of the three driest years, the vegetation drought response was analysed (Fig. 2c). Low soil moisture content is often accompanied by sunny and warm weather conditions, which enhance plant productivity as long as vegetation is not water-limited (Jolly et al., 2005). In this study, we were only interested in those severe droughts when the vegetation experienced a water deficit, identified through a low G_s. Therefore, we compared G_s during the day of the strongest soil moisture drought with the mean G_s for years without a soil moisture drought (Fig. 2c). Specifically, we tested if G_s for the drought years was at least 0.0025 m s^{-1} below the mean G_s for years without a soil moisture drought. This absolute value of 0.0025 m s^{-1} was introduced to remove sites from the data set that always had very low G_s, i.e. the sites (mostly grassland sites) that were always water-limited during the summer season (the season with a very low absolute soil moisture content and low year-to-year variability in G_s). Each year with a vegetation drought response is now referred to as a 'drought year' and each other year is a 'reference year'. These reference years thus include years without a soil moisture drought, years when the soil moisture drought was not severe enough to trigger vegetation reactions, and sites where the vegetation was similarly affected by reduced G_s during both drought years and non-drought years. Each site was included in the analyses that contained data for at least one drought year and at least three reference years. The final dataset after filtering contained 10 grassland sites with 13 droughts, and 47 forest sites with 80 droughts.

Step 4 Determine the onset of vegetation drought response.

For every drought year, we identified the day with the strongest vegetation drought response. This was the day with the strongest reduction in G_s over time (Fig. 2d).

We calculate ΔG_s as the change in G_s over time, as $\Delta G_{s,t} = \overline{G_{s,\,(t:(t+21))}} - \overline{G_{s,\,((t-21):t)}}$, where G_s is the 21-day rolling median G_s. Negative values for $\Delta G_{s,t}$ indicate that G_s decreased during the investigated weeks surrounding time t, and the most negative value of ΔG_s indicated the period with the strongest reduction in G_s. The onset of the vegetation drought response was defined as the day with the most negative ΔG_s before the strongest soil moisture drought (Fig. 2d). We assume that the strongest reduction in G_s is a response to the severe drought, however, it could also reflect for example logging or mowing rather than a drought response. Given the high number of sites, we do not forsee an effect of site-scale land-cover changes on our conclusions.

Step 5 Determine the response in remote sensing data.

For every drought year, we studied if the reduction in G_s was reflected in the optical and thermal infrared satellite indices (VI) (Fig. 2e). Therefore, we calculated the change in satellite data over time, the ΔVI. The ΔVI was calculated in a similar way as ΔG_s: $\Delta VI_t = \overline{VI_{(t:(t+21))}} - \overline{VI_{((t-21):t)}}$, where t is the day of the onset of vegetation drought response (as calculated in step 4). A negative ΔVI indicated that the satellite index reduced at the onset of vegetation drought response, while a positive

Table 1
Satellite data and indices used to analyse the vegetation drought response. The NDVI and LST (in bold) are the main focus of this manuscript, and the other indices are presented in the supplementary materials. LST_{min} and LST_{max} are the site-specific minimum and maximum LST in the studied time series.

	Index	Name	Formula	Refs.
Optical indices	**NDVI**	**Normalized Difference Vegetation Index**	$NDVI = \frac{(NIR - Red)}{(NIR + Red)}$	Kriegler et al. (1969)
	EVI	Enhanced Vegetation Index	$EVI = 2.5 * \frac{NIR - Red}{NIR + 6*Red - 7.5*Blue + 1}$	Huete and Liu (1994)
	NIRv	Near-infrared reflectance of vegetation	$NIRv = NDVI * NIR$	Badgley et al. (2017)
	SIPI	Structural Insensitive Photochemical Index	$SIPI = \frac{NIR - Blue}{NIR - Red}$	Penuelas et al. (1995)
Thermal infrared indices	**LST**	**Land Surface Temperature**		Jackson et al. (1977)
	$LST - T_a$	LST minus in-situ measured air temperature		Jackson et al. (1977)
	CWSI	Crop Water Stress Index	$CWSI = \frac{LST - LST_{min}}{LST_{max} - LST_{min}}$	Veysi et al. (2017)

ΔVI indicated that the satellite index increased at the onset of vegetation drought response.

2.5. Sensitivity tests

We tested the sensitivity of our results to the different choices in the methodology. First, we calculated the mean soil moisture over only layer 1 and 2 of ERA5-Land (0 – 30 cm), and we used soil moisture data to select the four driest years instead of the three driest years (step 1). Using the 0 – 30 cm reflects the water availability better for sites with low rooting depths. Second, we tested the effect of a different threshold value to remove sites that always have low G_s during the summer season (threshold values of 0, 0.001, 0.005, and 0.01 m s^{-1}, step 3). Third, we calculated the 14-day and 28-day rolling median G_s and 14-day and 28-day time interval to calculate ΔG_s (step 3 and 4). A different drought selection, threshold value, or moving window did occasionally changed the results for individual sites, but did not change the results and conclusion of the study (Supplementary Figs. 2–4).

3. Results

3.1. Land-atmosphere exchange of water, energy, and carbon during drought

Eddy covariance data for all 93 severe droughts in 57 sites showed that the strong reduction in G_s was accompanied by a reduction in the latent heat flux for forests (evaporation), an increase in the sensible heat flux, and a reduction in the vegetation carbon uptake (Fig. 3). This indicates that the drought-induced reduction of G_s reduced the land-atmosphere exchange of carbon and increased the sensible heat flux. For more than half of the grassland droughts, the latent heat increased at the onset of vegetation drought response. This increase in latent heat flux, despite the reduction in surface conductance, likely reflects the higher atmospheric vapor pressure deficit during drought. Do note that the latent heat flux and sensible heat flux were used to calculate G_s, and G_s is therefore not independent of the water and energy fluxes.

3.2. Drought years in satellite data

The soil moisture anomaly got more negative during the growing season with the strongest negative anomaly in August for both the forest and grassland sites (Fig. 4a, b). The onset of vegetation drought response was most often in mid-June to early-August for both forest and grassland sites, with the mean occurrence around middle July (forest) and the first week of July (grassland) (Fig. 4c, d). The onset of vegetation drought response was on average 40 days (forest) and 44 days (grassland) before the day of the strongest soil moisture drought.

The LST and NDVI had a contrasting response for forest and grassland sites. In the severe drought years, LST was substantially higher as compared to the reference years for both forest and grassland sites (Fig. 4e, f). On average, the median LST anomaly during drought years was + 1.2°C (grassland) and + 1.0°C (forest) in May and June, and + 3.4°C (grassland) and + 2.3°C (forest) in July and August. High LST was also observed before and after the onset of vegetation drought response. The NDVI had different responses for forest and grassland sites (Fig. 4g, h). For the forest sites, the site-to-site variability and the anomalies were small. Furthermore, the median forest NDVI anomaly was marginally positive in May (+ 0.010), while it was negative in August (– 0.012). On the contrary, in the grassland sites, the median drought anomaly was much larger in August (– 0.057) and negative during most of the season. The site-to-site variability in NDVI anomaly in grassland was larger than for forest sites, and the number of grassland droughts in our dataset is much lower compared to the number of forest droughts. Therefore, the NDVI anomalies for grassland were less often statistically significantly from zero for a similar or larger anomaly value.

Other thermal indices, the LST – T_A and CWSI, showed a similar anomaly in drought years as the LST (Supplementary Fig. 5a-d). For both forests and grasslands, LST – T_A and CWSI had a positive anomaly during the drought years for most of the growing season. Other optical indices, the EVI, NIRv, and SIPI, showed a similar response as the NDVI (Supplementary Fig. 5e-j). The absolute anomalies in all optical indices is larger for grasslands than for forests throughout most of the summer season. On average, the median absolute anomalies throughout the growing season in are 13 – 17 times higher for grassland sites compared to forest sites. Also, the spatial variability in anomalies is larger for grassland sites compared to forest sites, the median standard deviation of the anomalies throughout the growing season is 1.6 – 2 times higher for grassland sites compared to forest sites.

Fig. 4 shows how thermal and optical data reflected drought years. The figure reflects that the optical indices show a stronger response to grassland droughts than to forest droughts, while the response in thermal data and indices is comparable for forests and grasslands. This supports our hypothesis that drought-induced changes in forest and grassland G_s have a contrasting response in the satellite data. To further study this hypothesis, we focus on the weeks before and after the onset of the vegetation drought response. For all drought years, we calculated

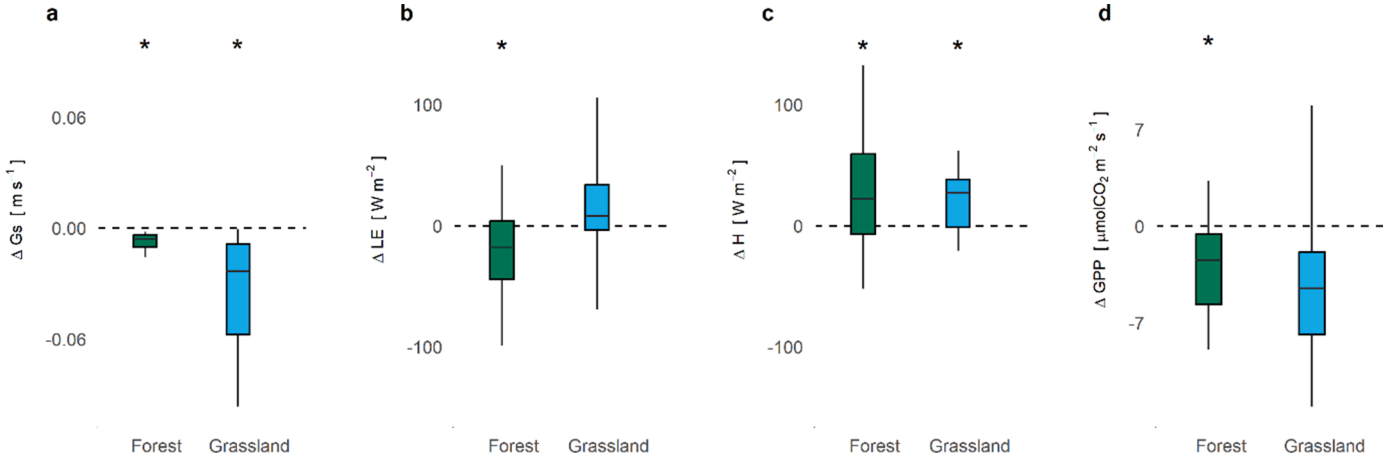

Fig. 3. Land-atmosphere exchange of water, energy, and carbon during drought. A reduction in (a) surface conductance (G_s) impacts the fluxes of (b) evaporation (LE), (c) sensible heat (H), and (d) and gross primary productivity (GPP). Data for 93 droughts in 57 eddy covariance sites (47 forest sites and 10 grassland sites). The values are calculated as the mean value in the three weeks before minus three weeks after the onset of vegetation drought response for each individual drought event. The boxes show the 25th – 75th percentile over the droughts at all forest and grassland sites, and the lines represent the 5th – 95th percentile range. A * indicate that the change is significantly different from zero at $p \leq 0.05$.

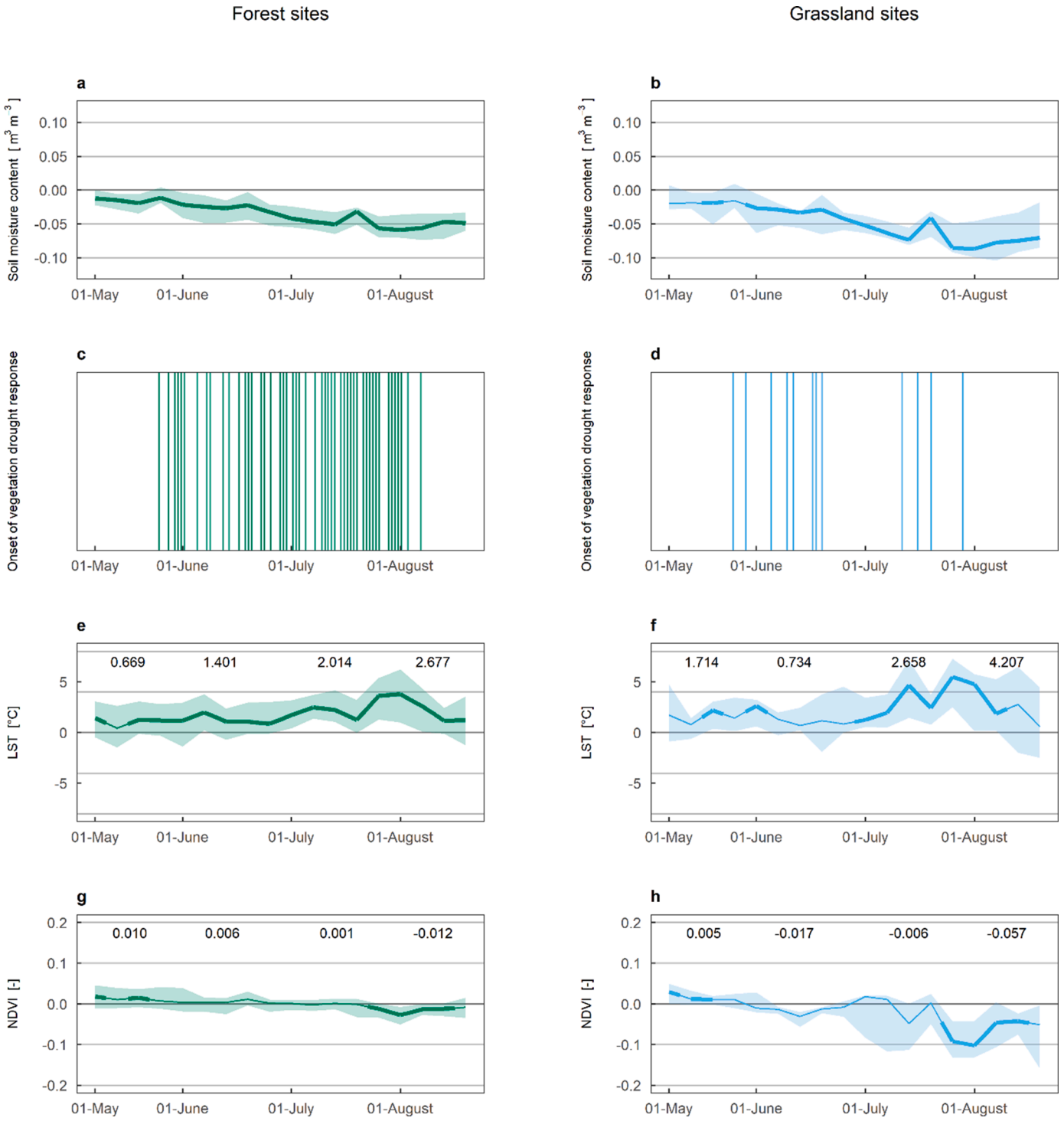

Fig. 4. Composite of drought anomalies in remote sensing data across all sites. The median difference in the soil moisture content for the drought years and reference years for (a) forest sites and (b) grassland sites. The timing of the onset of the vegetation drought response for all droughts detected at all (c) forest sites and (d) grassland sites. (e-h) Median differences in the drought years and reference years for the (e-f) land surface temperature (LST), and (g-h) normalized difference vegetation index (NDVI). For each of the 47 forest sites and 10 grassland sites, the mean satellite signal over all drought years is compared to the mean signal over all reference years. The numbers indicate the median anomaly for each calendar month, the shaded areas represent the inter-quartile range of responses, and a thick line indicates that the anomaly is significantly different from zero ($p \leq 0.05$).

the change in the remote sensing data between the three weeks before and after the onset of the vegetation drought response.

3.3. The onset of vegetation drought response in satellite data

The surface conductance G_s decreased at the onset of the vegetation drought response (Fig. 5a). This was by construction, because the onset of vegetation drought response was defined as the day with strongest reduction in G_s. The magnitude of the reduction in G_s was lower for forest sites ($-\ 0.007 \pm 0.006$ m s^{-1}) compared to grassland sites ($-\ 0.037 \pm 0.036$ m s^{-1}). At the onset of the vegetation drought response, ΔLST was positive; the LST increased during the weeks when G_s

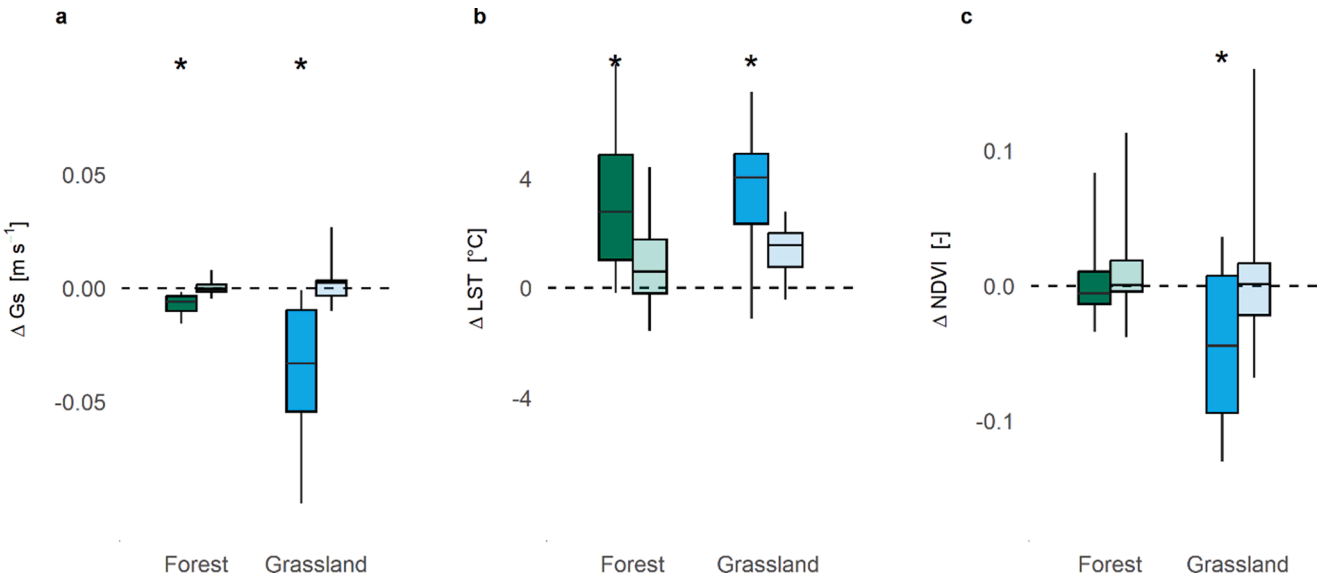

Fig. 5. The onset of vegetation drought response reflected in satellite data. (a) Changes in the surface conductance G_s at the onset of the vegetation drought response from in-situ eddy covariance data. Changes in (b) land surface temperature (LST), and (c) normalized difference vegetation index (NDVI) derived from satellite data. The values are calculated as the mean value in the three weeks before minus three weeks after the onset of vegetation drought response for each individual drought event. For comparison, the figure includes the respective differences calculated with the same days of the drought year, but for the reference years, in light green and light blue. The boxes show the 25^{th} – 75^{th} percentile over the droughts at all forest and grassland sites, and the lines represent the 5^{th} – 95^{th} percentile range. A $*$ indicates that the change is significantly different from zero at $p \leq 0.05$.

decreased (Fig. 5b). The mean increase in LST was of similar magnitude for forest (3.1°C) and grassland (3.5°C) sites. The mean ΔNDVI was slightly positive for forest sites, but negative grassland sites (Fig. 5c). The mean increase in forest NDVI was not significant (0.007), while the NDVI showed a significant decrease for grassland sites (− 0.048). For forest sites, ΔNDVI was negative for 61% of the severe droughts at all sites, while for grasslands, ΔNDVI was negative for 73% of the severe droughts. Fig. 5 also includes the Δ-values for the similar period in the reference years. For G_s and NDVI, the reference responses were centred around zero. This indicates that, overall, we expect no strong confounding effects of seasonality in the results. For LST, ΔLST was positive during reference years, which shows the effect of seasonality. The increase in LST in reference year (0.9°C) is however much smaller than the mean increase in drought years (3.2°C).

An increase in LST can reflect a decrease in the evaporative fraction (a decrease in G_s) (Mallick et al., 2022), but an increase in LST can also reflect an increase in incoming shortwave radiation or air temperature (Panwar and Kleidon, 2022). For each site, we calculated the partial correlation between the rolling median LST and G_s, that accounted for air temperature and incoming radiation. We did this to test if the increase in LST was correlated to the decrease in G_s, or only to the changes in temperature and radiation. The partial correlation was calculated for the 6 weeks centred around the onset of the vegetation drought response. For 58 out of 90 droughts (64 %), the LST significantly increased with decreasing G_s, also when accounting for temperature and radiation. This confirms that for most sites, the LST reflects drought-induced reductions in G_s. Land cover, and meteorological and climate variables did not explain why some sites had a small or a non-significant correlation between LST and G_s. The results, as presented in Fig. 5, were not different between sites with or without a significant partial correlation between LST and G_s.

Most other thermal infrared and optical indices had a similar result as the LST and NDVI (Supplementary Fig. 6). The CWSI, which was calculated from the LST, had a very similar response to the reduction in G_s as the LST: it increased at the onset of vegetation drought response for both forest and grassland sites (Supplementary Fig. 6b). The LST $-T_a$ showed no clear response. For both forest and grassland sites, the ΔLST $-T_a$ was more positive during the vegetation drought onset compared to reference years (Supplementary Fig. 6c). However, there was a large variability in the response, and for 33 % of the grassland sites and 54 % of the forest sites, the LST $- T_a$ decreased at the onset of vegetation drought response. LST based indices are considered to be a better indicator of vegetation drought stress, because they are less sensitive to meteorological variables (Neinavaz et al., 2021). On the other hand, T_a increases with LST and therefore, their difference does not go beyond a high limit. The spatial mismatch between the satellite measurements of LST and the ground measurement of T_a might explain the weak and variable response of LST $- T_a$ to changes in canopy conductance in this study. Other optical indices, the EVI, NIRv, and SIPI responded similarly as the NDVI (Supplementary Fig.d-f). The EVI and NIRv decreased during the onset of vegetation drought response, and the absolute decrease was larger for grassland sites compared to forest sites. The SIPI did not reflect any change for forests and increased for grassland sites. This indicated that for forests, no or only minor changes could be detected in the structure and greenness of the vegetation.

4. Discussion

The current analysis revealed that the different drought response strategies of forest and grassland are reflected in the satellite data. For both forest and grassland sites, LST increased at the timing of drought-induced reductions in G_s. During drought, persistent water stress in combination with high vapor pressure deficit and radiative heating, triggers a decline in G_s and evaporative fraction (Grossiord et al., 2020). This leads to a further increase in vapor pressure deficit within vegetation, and an increase in sensible heat flux, air temperature, and the LST (Mallick et al., 2022). For the forest sites, the reduction in G_s was accompanied by a minor reduction in NDVI and other optical indices. This confirms that most forest sites had a strong stomatal regulation to reduce water loss, while there were no significant changes in their canopy structure and greenness. For the grassland sites, the decrease in G_s was accompanied by a strong reduction in the NDVI and strong changes in other optical indices. This reflects that the decrease in grassland G_s was (partly) regulated by a decrease in the grassland's green leaf area. The marginally negative forest NDVI anomaly at the end of the summer (Fig. 4) and slight decrease in NDVI at the onset of drought

response for 60 % of the sites (Fig. 5) also indicates the possibility of change in forest color or structure (e.g. leaf angle) to some extent during the course of the severe droughts. Here, we attribute the differences between forest and grassland sites to their different drought coping strategies. The results might, however, be confounded by the effect of different climate regimes and drought characteristics. For example, most forest sites lie in mesic regions, while the grassland sites are equally spread over arid and mesic regions. We tested our research hypothesis on arid (aridity index > 1) and mesic (aridity index < 1) sites separately, but this did not change the results and conclusion of our study. Furthermore, we only analysed severe droughts and excluded sites (mostly grassland sites) that were always water-limited during the dry season. Our results do therefore not reflect the grassland and forest response to regular dry conditions.

This study generalised the tree and grassland drought responses, however, there is no uniform drought response across species and sites. For example, different drought adaptation strategies exist between tree species, such as a stronger stomatal regulation for leaves versus needles (Wolf et al., 2013), or a higher sensitivity of Norway spruce to drought compared to pine because of their different rooting depths (Schuldt et al., 2020; Treml et al., 2021). For grasslands, the degree of stomatal control also varies with species (Signarbieux and Feller, 2011). In our study, some sites have a weak satellite response while they experience a strong reduction in G_s, while other sites show an increase in satellite indices when a decrease was expected. The different forest leaf types explained part of the variability in the forest NDVI response: for needleleaf sites, the ΔNDVI at the onset of vegetation drought response was slightly positive (ΔNDVI $=$ 0.002), while the NDVI decreased for broadleaf sites (ΔNDVI $=-$ 0.009) (Supplementary Fig. 7). However, for both forest types, the decrease at the onset of drought response is lower than the change in reference years. Meteorological or climate variables did not explain the variability in G_s or satellite-based drought response.

In this study, we assign the presence and absence of a satellite signal to the canopy-scale vegetation drought response. However, the absence of a NDVI signal in forest can also be related to the saturation of the remote sensing signal in forests (Huang et al., 2021), rather than the absence of a visible vegetation drought response. Independent of whether it is related to the forest drought strategy, or to the saturation of the remote sensing signal, this study confirms and explains that optical indices such as the NDVI or NIRv do not or only weakly reflect drought stress in temperate forests (Bachmair et al., 2018; Hoek van Dijke et al., 2019; Vicca et al., 2016; Xu et al., 2018; Zhang et al., 2016). This makes optical vegetation indices less suitable to study the forest drought stress and drought-related changes in water, energy, and carbon fluxes. On the other hand, LST and CWSI increased at the onset of vegetation drought response for both forest and grassland sites which demonstrates their suitability for drought stress monitoring.

Recently launched satellites and upcoming missions provide a great opportunity for global assessments of vegetation drought stress. These future missions include new sun-induced fluorescence missions (FLEX), high spatial resolution thermal missions (LSTM, Trishna, and SBG), and hyperspectral missions (EnMAP and CHIME). These satellite sensors for example allow for studying specific narrow waveband measurements that reflect the xanthophyll pigments (PRI indices, Gamon et al. (1992)) or the abundance of chlorophyll (CARI indices, Kim et al., 1994), and high resolution assessment of sun-induced fluorescence (Cao et al., 2021) and land surface temperature. Using the different satellite data in a synergistic way (Berger et al., 2022) will improve future assessments of the vegetation drought response of forests and grasslands. Furthermore, the high resolution satellite data, in combination with high quality flux measurements across the Earth's surface, provides the opportunity to further enhance the understanding of how satellite data reflect the vegetation drought response, as well as the drought-related changes in water, energy, and carbon fluxes for different ecosystems and plant functional types.

5. Conclusions

In our study we investigated how the different drought response strategies of temperate forests and grasslands are reflected in remote sensing data. In summary, we found that:

1 For forests, at the timing of drought-induced reduction in G_s, the LST increased. However, the response in the NDVI and other optical indices was only minor, or even absent for 40% of the forest sites. This likely reflects the trees' strong stomatal control to reduce water loss during severe droughts.
2 For grasslands, the drought-induced reduction in G_s was accompanied by a strong response in the NDVI and other optical indices. This reflects that the decline in G_s was partly regulated by a reduction in green biomass. Similar to the forest sites, the reduction in G_s was accompanied by an increase in LST.

These results indicate that contrasting forest and grassland drought response strategies are found over large regions. The combination of optical and thermal remote sensing can be employed to further improve the understanding of large-scale vegetation drought responses in different climates and plant functional types, and this could help to improve the drought predictive responses in land surface models. Furthermore, we conclude that a different satellite monitoring strategy is required to monitor the vegetation drought response and to ensure accurate inference on the implications for land-atmosphere fluxes of water, energy, and carbon.

Declaration of Competing Interest

The authors declare no competing interests.

Data availability

The eddy covariance, soil moisture, and satellite data that was used in these analysis is all openly available or available on request from the data owners.

Acknowledgement

This research was supported by the Luxembourg National Research Fund (FNR) (PRIDE15/10623093/HYDROCSI) and by the German Research Foundation (Emmy Noether grant 391059971). The funding for the AmeriFlux data portal was provided by the U.S. Department of Energy Office of Science

Supplementary materials

Supplementary material associated with this article can be found, in the online version, at doi:10.1016/j.agrformet.2023.109635.

References

Anderegg, W.R., Schwalm, C., Biondi, F., Camarero, J.J., Koch, G., Litvak, M., Ogle, K., Shaw, J.D., Shevliakova, E., Williams, A.P., Wolf, A., Ziaco, E., Pacala, S., 2015. FOREST ECOLOGY. Pervasive drought legacies in forest ecosystems and their implications for carbon cycle models. Science 349 (6247), 528–532. https://doi.org/10.1126/science.aab1833.

Bachmair, S., Tanguy, M., Hannaford, J., Stahl, K., 2018. How well do meteorological indicators represent agricultural and forest drought across Europe? Environ. Res. Lett. 13 (3), 034042 https://doi.org/10.1088/1748-9326/aaafda.

Badgley, G., Field, C.B., Berry, J.A., 2017. Canopy near-infrared reflectance and terrestrial photosynthesis. Sci. Adv. 3 (3), e1602244 https://doi.org/10.1126/sciadv.1602244.

Berger, K., Machwitz, M., Kycko, M., Kefauver, S.C., Van Wittenberghe, S., Gerhards, M., Verrelst, J., Atzberger, C., van der Tol, C., Damm, A., Rascher, U., Herrmann, I., Paz, V.S., Fahrner, S., Pieruschka, R., Prikaziuk, E., Buchaillot, M.L., Halabuk, A., Celesti, M., Schlerf, M., 2022. Multi-sensor spectral synergies for crop stress

detection and monitoring in the optical domain: A review. Remote Sens. Environ. 280, 113198 https://doi.org/10.1016/j.rse.2022.113198.
Brodribb, T.J., Powers, J., Cochard, H., Choat, B., 2020. Hanging by a thread? Forests and drought. Science 368 (6488), 261–266. https://doi.org/10.1126/science.aat7631.
Buitink, J., Swank, A.M., van der Ploeg, M., Smith, N.E., Benninga, H.J.F., van der Bolt, F., Carranza, C.D.U., Koren, G., van der Velde, R., Teuling, A.J., 2020. Anatomy of the 2018 agricultural drought in the Netherlands using *in situ* soil moisture and satellite vegetation indices. Hydrol. Earth Syst. Sci. 24 (12), 6021–6031. https://doi.org/10.5194/hess-24-6021-2020.
Buras, A., Rammig, A., Zang, S., 2020. Quantifying impacts of the 2018 drought on European ecosystems in comparison to 2003. Biogeosciences 17 (6), 1655–1672. https://doi.org/10.5194/bg-17-1655-2020.
Cao, J., An, Q., Zhang, X., Xu, S., Si, T., Niyogi, D., 2021. Is satellite sun-induced chlorophyll fluorescence more indicative than vegetation indices under drought condition? Sci. Total Environ. 792, 148396 https://doi.org/10.1016/j.scitotenv.2021.148396.
Warm Winter 2020 Team, & ICOS Ecosystem Thematic Centre. (2022). Warm Winter 2020 ecosystem eddy covariance flux product for 73 stations in FLUXNET-Archive format - release 2022-1 (Version 1.0). doi:10.18160/2G60-ZHAK.
Centre, D.T.A.I.E.T. (2020). Drought-2018 ecosystem eddy covariance flux product for 52 stations in FLUXNET-Archive format. doi:10.18160/YVR0-4898h.
Choat, B., Brodribb, T.J., Brodersen, C.R., Duursma, R.A., López, R., Medlyn, B.E., 2018. Triggers of tree mortality under drought. Nature 558 (7711), 531–539. https://doi.org/10.1038/s41586-018-0240-x.
Ciais, P., Reichstein, M., Viovy, N., Granier, A., Ogée, J., Allard, V., Aubinet, M., Buchmann, N., Bernhofer, C., Carrara, A., Chevallier, F., De Noblet, N., Friend, A.D., Friedlingstein, P., Grünwald, T., Heinesch, B., Keronen, P., Knohl, A., Krinner, G., Valentini, R., 2005. Europe-wide reduction in primary productivity caused by the heat and drought in 2003. Nature 437 (7058), 529–533. https://doi.org/10.1038/nature03972.
De Kauwe, M.G., Kala, J., Lin, Y.S., Pitman, A.J., Medlyn, B.E., Duursma, R.A., Abramowitz, G., Wang, Y.P., Miralles, D.G., 2015. A test of an optimal stomatal conductance scheme within the CABLE land surface model. Geosci. Model Dev. 8 (2), 431–452. https://doi.org/10.5194/gmd-8-431-2015.
De Kauwe, M.G., Medlyn, B.E., Knauer, J., Williams, C.A., 2017. Ideas and perspectives: how coupled is the vegetation to the boundary layer? Biogeosciences 14 (19), 4435–4453. https://doi.org/10.5194/bg-14-4435-2017.
Ekinzog, E.K., Schlerf, M., Kraft, M., Werner, F., Riedel, A., Rock, G., Mallick, K., 2022. Revisiting crop water stress index based on potato field experiments in Northern Germany. Agric. Water Manage. 269, 107664 https://doi.org/10.1016/j.agwat.2022.107664.
Franks, P.J., Bonan, G.B., Berry, J.A., Lombardozzi, D.L., Holbrook, N.M., Herold, N., Oleson, K.W., 2018. Comparing optimal and empirical stomatal conductance models for application in Earth system models. Glob. Change Biol. 24 (12), 5708–5723. https://doi.org/10.1111/gcb.14445.
Fu, Z., Ciais, P., Prentice, I.C., Gentine, P., Makowski, D., Bastos, A., Luo, X., Green, J.K., Stoy, P.C., Yang, H., Hajima, T., 2022. Atmospheric dryness reduces photosynthesis along a large range of soil water deficits. Nat. Commun. 13 (1), 989. https://doi.org/10.1038/s41467-022-28652-7.
Gamon, J.A., Peñuelas, J., Field, C.B., 1992. A narrow-waveband spectral index that tracks diurnal changes in photosynthetic efficiency. Remote Sens. Environ. 41 (1), 35–44. https://doi.org/10.1016/0034-4257(92)90059-S.
Gerhards, M., Rock, G., Schlerf, M., Udelhoven, T., 2016. Water stress detection in potato plants using leaf temperature, emissivity, and reflectance. Int. J. Appl. Earth Obs. Geoinf. 53, 27–39. https://doi.org/10.1016/j.jag.2016.08.004.
Gerhards, M., Schlerf, M., Mallick, K., Udelhoven, T., 2019. Challenges and future perspectives of multi-/hyperspectral thermal infrared remote sensing for crop water-stress detection: a review. Remote. Sens. 11 (10), 1240. https://doi.org/10.3390/rs11101240.
Graf, A., Klosterhalfen, A., Arriga, N., Bernhofer, C., Bogena, H., Bornet, F., Brüggemann, N., Brümmer, C., Buchmann, N., Chi, J., Chipeaux, C., Cremonese, E., Cuntz, M., Dušek, J., El-Madany, T.S., Fares, S., Fischer, M., Foltýnová, L., Gharun, M., Vereecken, H., 2020. Altered energy partitioning across terrestrial ecosystems in the European drought year 2018. Philos. Trans. R. Soc. B Biol. Sci. 375 (1810), 20190524 https://doi.org/10.1098/rstb.2019.0524.
Granier, A., Reichstein, M., Bréda, N., Janssens, I.A., Falge, E., Ciais, P., Grünwald, T., Aubinet, M., Berbigier, P., Bernhofer, C., Buchmann, N., Facini, O., Grassi, G., Heinesch, B., Ilvesniemi, H., Keronen, P., Knohl, A., Köstner, B., Lagergren, F., Wang, Q., 2007. Evidence for soil water control on carbon and water dynamics in European forests during the extremely dry year: 2003. Agric. For. Meteorol. 143 (1), 123–145. https://doi.org/10.1016/j.agrformet.2006.12.004.
Grossiord, C., Buckley, T.N., Cernusak, L.A., Novick, K.A., Poulter, B., Siegwolf, R.T.W., Sperry, J.S., McDowell, N.G., 2020. Plant responses to rising vapor pressure deficit [10.1111/nph.16485]. New Phytol. 226 (6), 1550–1566. https://doi.org/10.1111/nph.16485.
Haberstroh, S., Werner, C., Grün, M., Kreuzwieser, J., Seifert, T., Schindler, D., Christen, A., 2022. Central European 2018 hot drought shifts scots pine forest to its tipping point. Plant Biol. 24 (7), 1186–1197. https://doi.org/10.1111/plb.13455.
Herrera-Estrada, J.E., Martinez, J.A., Dominguez, F., Findell, K.L., Wood, E.F., Sheffield, J., 2019. Reduced moisture transport linked to drought propagation across North America. Geophys. Res. Lett. 46 (10), 5243–5253. https://doi.org/10.1029/2019GL082475.
Hoek van Dijke, A.J., Mallick, K., Teuling, A.J., Schlerf, M., Machwitz, M., Hassler, S.K., Blume, T., Herold, M., 2019. Does the Normalized Difference Vegetation Index explain spatial and temporal variability in sap velocity in temperate forest ecosystems? Hydrol. Earth Syst. Sci. 23 (4), 2077–2091. https://doi.org/10.5194/hess-23-2077-2019.
Huang, S., Tang, L., Hupy, J.P., Wang, Y., Shao, G., 2021. A commentary review on the use of normalized difference vegetation index (NDVI) in the era of popular remote sensing. J. For. Res. 32 (1), 1–6. https://doi.org/10.1007/s11676-020-01155-1.
Huete, A.R., Liu, H.Q., 1994. An error and sensitivity analysis of the atmospheric- and soil-correcting variants of the NDVI for the MODIS-EOS. IEEE Trans. Geosci. Remote Sens. 32 (4), 897–905. https://doi.org/10.1109/36.298018.
Jackson, R.D., Reginato, R.J., Idso, S.B., 1977. Wheat canopy temperature: a practical tool for evaluating water requirements. Water Resour. Res. 13 (3), 651–656. https://doi.org/10.1029/WR013i003p00651.
Jolly, W.M., Dobbertin, M., Zimmermann, N.E., Reichstein, M., 2005. Divergent vegetation growth responses to the 2003 heat wave in the Swiss Alps. Geophys. Res. Lett. (18), 32. https://doi.org/10.1029/2005GL023252.
Kannenberg, S.A., Novick, K.A., Alexander, M.R., Maxwell, J.T., Moore, D.J.P., Phillips, R.P., Anderegg, W.R.L., 2019. Linking drought legacy effects across scales: From leaves to tree rings to ecosystems. Glob. Change Biol. 25 (9), 2978–2992. https://doi.org/10.1111/gcb.14710.
Kong, J., Ryu, Y., Liu, J., Dechant, B., Rey-Sanchez, C., Shortt, R., Szutu, D., Verfaillie, J., Houborg, R., Baldocchi, D.D., 2022. Matching high resolution satellite data and flux tower footprints improves their agreement in photosynthesis estimates. Agric. For. Meteorol. 316, 108878 https://doi.org/10.1016/j.agrformet.2022.108878.
Krasnova, A., Mander, Ü., Noe, S.M., Uri, V., Krasnov, D., Soosaar, K., 2022. Hemiboreal forests' CO2 fluxes response to the European 2018 heatwave. Agric. For. Meteorol. 323, 109042 https://doi.org/10.1016/j.agrformet.2022.109042.
Kriegler, F., Malila, W., Nalepka, R., Richardson, W., 1969. Preprocessing transformations and their effects on multispectral recognition. Remote Sens. Environ. VI, 97.
Lansu, E.M., van Heerwaarden, C.C., Stegehuis, A.I., Teuling, A.J., 2020. Atmospheric Aridity and apparent soil moisture drought in european forest during heat waves. Geophys. Res. Lett. 47 (6), e2020GL087091 https://doi.org/10.1029/2020GL087091.
Lin, Y.S., Medlyn, B.E., Duursma, R.A., Prentice, I.C., Wang, H., Baig, S., Eamus, D., de Dios, Vr., Mitchell, P., Ellsworth, D.S., de Beeck, M.O., Wallin, G., Uddling, J., Tarvainen, L., Linderson, M.L., Cernusak, L.A., Nippert, J.B., Ocheltree, T.W., Tissue, D.T., Wingate, L., 2015. Optimal stomatal behaviour around the world. Nat. Clim. Change. 5 (5), 459–464. https://doi.org/10.1038/nclimate2550.
Mallick, K., Baldocchi, D., Jarvis, A., Hu, T., Trebs, I., Sulis, M., Bhattarai, N., Bossung, C., Eid, Y., Cleverly, J., Beringer, J., Woodgate, W., Silberstein, R., Hinko-Najera, N., Meyer, W.S., Ghent, D., Szantoi, Z., Boulet, G., Kustas, W.P., 2022. Insights into the aerodynamic versus radiometric surface temperature debate in thermal-based evaporation modeling. Geophys. Res. Lett. 49 (15), e2021GL097568 https://doi.org/10.1029/2021GL097568.
Mallick, K., Toivonen, E., Trebs, I., Boegh, E., Cleverly, J., Eamus, D., Koivusalo, H., Drewry, D., Arndt, S.K., Griebel, A., Beringer, J., Garcia, M., 2018. Bridging thermal infrared sensing and physically-based evapotranspiration modeling: from theoretical implementation to validation across an aridity gradient in australian ecosystems. Water Resour. Res. 54 (5), 3409–3435. https://doi.org/10.1029/2017wr021357.
Mallick, K., Trebs, I., Boegh, E., Giustarini, L., Schlerf, M., Drewry, D.T., Hoffmann, L., Von Randow, C., Kruijt, B., Araùjo, A., Saleska, S., Ehleringer, J.R., Domingues, T.F., Ometto, J.P.H.B., Nobre, A.D., Luiz Leal De Moraes, O., Hayek, M., William Munger, J., Wofsy, S.C., 2016. Canopy-scale biophysical controls of transpiration and evaporation in the Amazon Basin. Hydrol. Earth Syst. Sci. 20 (10), 4237–4264. https://doi.org/10.5194/hess-20-4237-2016.
Mekonnen, Z.A., Grant, R.F., Schwalm, C., 2017. Carbon sources and sinks of North America as affected by major drought events during the past 30 years. Agric. For. Meteorol. 244-245, 42–56. https://doi.org/10.1016/j.agrformet.2017.05.006.
Miralles, D.G., Gentine, P., Seneviratne, S.I., Teuling, A.J., 2019. Land–atmospheric feedbacks during droughts and heatwaves: state of the science and current challenges. Ann. N.Y. Acad. Sci. 1436 (1), 19–35. https://doi.org/10.1111/nyas.13912.
Muñoz Sabater, J., 2019. ERA5-Land Monthly Averaged Data from 1981 to Present. accessed January 2020. Copernicus Climate Change Service (C3S) Climate Data Store (CDS). https://doi.org/10.24381/cds.68d2bb3.
Neinavaz, E., Schlerf, M., Darvishzadeh, R., Gerhards, M., Skidmore, A.K., 2021. Thermal infrared remote sensing of vegetation: current status and perspectives. Int. J. App. Earth Obs. Geoinf. 102, 102415. https://doi.org/10.1016/j.jag.2021.102415.
Nemani, R.R., Running, S.W., 1989. Estimation of regional surface resistance to evapotranspiration from NDVI and thermal-IR AVHRR data. J. Appl. Meteorol. Climatol. 28 (4), 276–284. https://doi.org/10.1175/1520-0450(1989)028<0276:EORSRT>2.0.CO;2.
O, S., Bastos, A., Reichstein, M., Li, W., Denissen, J., Graefen, H., Orth, R., 2022. The role of climate and vegetation in regulating drought–heat extremes. J. Clim. 35 (17), 5677–5685. https://doi.org/10.1175/JCLI-D-21-0675.1.
Obladen, N., Dechering, P., Skiadaresis, G., Tegel, W., Keßler, J., Höllerl, S., Kaps, S., Hertel, M., Dulamsuren, C., Seifert, T., Hirsch, M., Seim, A., 2021. Tree mortality of European beech and Norway spruce induced by 2018-2019 hot droughts in central Germany. Agric. For. Meteorol. 307, 108482 https://doi.org/10.1016/j.agrformet.2021.108482.
Oliver, R.J., Mercado, L.M., Clark, D.B., Huntingford, C., Taylor, C.M., Vidale, P.L., McGuire, P.C., Todt, M., Folwell, S., Shamsudheen Semeena, V., Medlyn, B.E., 2022. Improved representation of plant physiology in the JULES-vn5.6 land surface model: photosynthesis, stomatal conductance and thermal acclimation. Geosci. Model Dev. 15 (14), 5567–5592. https://doi.org/10.5194/gmd-15-5567-2022.

Panwar, A., Kleidon, A., 2022. Evaluating the response of diurnal variations in surface and air temperature to evaporative conditions across vegetation types in FLUXNET and ERA5. J. Clim. 35 (19), 2701–2728. https://doi.org/10.1175/JCLI-D-21-0345.1.

Pastorello, G., Trotta, C., Canfora, E., Chu, H., Christianson, D., Cheah, Y.W., Poindexter, C., Chen, J., Elbashandy, A., Humphrey, M., Isaac, P., Polidori, D., Ribeca, A., van Ingen, C., Zhang, L., Amiro, B., Ammann, C., Arain, M.A., Ardö, J., Papale, D., 2020. The FLUXNET2015 dataset and the ONEFlux processing pipeline for eddy covariance data. Sci. Data 7 (1), 225. https://doi.org/10.1038/s41597-020-0534-3.

Paw, U., K, T., Gao, W., 1988. Applications of solutions to non-linear energy budget equations. Agric. For. Meteorol. 43 (2), 121–145. https://doi.org/10.1016/0168-1923(88)90087-1.

Penuelas, J., Baret, F., Filella, I., 1995. Semi-empirical indices to assess carotenoids/chlorophyll a ratio from leaf spectral reflectance. Photosynthetica 31 (2), 221–230.

Peters, W., van der Velde, I.R., van Schaik, E., Miller, J.B., Ciais, P., Duarte, H.F., van der Laan-Luijkx, I.T., van der Molen, M.K., Scholze, M., Schaefer, K., Vidale, P.L., Verhoef, A., Wårlind, D., Zhu, D., Tans, P.P., Vaughn, B., White, J.W.C., 2018. Increased water-use efficiency and reduced CO2 uptake by plants during droughts at a continental scale. Nat. Geosci. 11 (10), 744–748. https://doi.org/10.1038/s41561-018-0212-7.

Pranindita, A., Wang-Erlandsson, L., Fetzer, I., Teuling, A.J., 2021. Moisture recycling and the potential role of forests as moisture source during European heatwaves. Clim. Dyn. https://doi.org/10.1007/s00382-021-05921-7.

Quiring, S.M., Ganesh, S., 2010. Evaluating the utility of the Vegetation Condition Index (VCI) for monitoring meteorological drought in Texas. Agric. For. Meteorol. 150 (3), 330–339. https://doi.org/10.1016/j.agrformet.2009.11.015.

Salehi-Lisar, S.Y., Bakhshayeshan-Agdam, H., 2016. In: Hossain, M., Wani, S., Bhattacharjee, S., Burritt, D., Tran, LS. (Eds.), Drought Stress Tolerance in Plants, 1. Springer, Cham. https://doi.org/10.1007/978-3-319-28899-4_1.

Schuldt, B., Buras, A., Arend, M., Vitasse, Y., Beierkuhnlein, C., Damm, A., Gharun, M., Grams, T.E.E., Hauck, M., Hajek, P., Hartmann, H., Hiltbrunner, E., Hoch, G., Holloway-Phillips, M., Körner, C., Larysch, E., Lübbe, T., Nelson, D.B., Rammig, A., Kahmen, A., 2020. A first assessment of the impact of the extreme 2018 summer drought on Central European forests [Article]. Basic Appl. Ecol. 45, 86–103. https://doi.org/10.1016/j.baae.2020.04.003.

Schumacher, D.L., Keune, J., van Heerwaarden, C.C., Vilà-Guerau de Arellano, J., Teuling, A.J., Miralles, D.G., 2019. Amplification of mega-heatwaves through heat torrents fuelled by upwind drought. Nat. Geosci. 12 (9), 712–717. https://doi.org/10.1038/s41561-019-0431-6.

Senf, C., Buras, A., Zang, C.S., Rammig, A., Seidl, R., 2020. Excess forest mortality is consistently linked to drought across Europe. Nat. Commun. 11 (1), 6200. https://doi.org/10.1038/s41467-020-19924-1.

Senf, C., Seidl, R., 2021. Persistent impacts of the 2018 drought on forest disturbance regimes in Europe. Biogeosciences 18 (18), 5223–5230. https://doi.org/10.5194/bg-18-5223-2021.

Signarbieux, C., Feller, U., 2011. Non-stomatal limitations of photosynthesis in grassland species under artificial drought in the field. Environ. Exp. Bot. 71 (2), 192–197. https://doi.org/10.1016/j.envexpbot.2010.12.003.

Teuling, A.J., Seneviratne, S.I., Stöckli, R., Reichstein, M., Moors, E., Ciais, P., Luyssaert, S., van den Hurk, B., Ammann, C., Bernhofer, C., Dellwik, E., Gianelle, D., Gielen, B., Grünwald, T., Klumpp, K., Montagnani, L., Moureaux, C., Sottocornola, M., Wohlfahrt, G., 2010. Contrasting response of European forest and grassland energy exchange to heatwaves. Nat. Geosci. 3 (10), 722–727. https://doi.org/10.1038/ngeo950.

Treml, V., Mašek, J., Tumajer, J., Rydval, M., Čada, V., Ledvinka, O., Svoboda, M., 2021. Trends in climatically driven extreme growth reductions of Picea abies and Pinus sylvestris in Central Europe. Glob. Change Biol. https://doi.org/10.1111/gcb.15922.

van Hateren, T.C., Chini, M., Matgen, P., Teuling, A.J., 2021. Ambiguous agricultural drought: characterising soil moisture and vegetation droughts in europe from earth observation. Remote Sens. 13 (10), 1990. https://doi.org/10.3390/rs13101990.

Kim, M.S., Daughtry, C.S.T., Chappelle, E.W., McMurtrey, J.E., Walthall, C.L. The Use of High Spectral Resolution Bands for Estimating Absorbed Photosynthetically Active Radiation (APAR). Proceedings of the 6th Symposium on Physical Measurements and Signatures in Remote Sensing, CNES, January 1994.

Vermote, E., & Wolfe, R. (2021a). MODIS/Aqua surface reflectance daily L2G global 1km and 500m SIN grid V061 doi:10.5067/MODIS/MYD09GA.061.

Vermote, E., & Wolfe, R. (2021b). MODIS/Terra surface reflectance daily L2G global 1km and 500m SIN Grid V061 doi:10.5067/MODIS/MOD09GA.061.

Veysi, S., Naseri, A.A., Hamzeh, S., Bartholomeus, H., 2017. A satellite based crop water stress index for irrigation scheduling in sugarcane fields. Agric. Water Manage. 189, 70–86. https://doi.org/10.1016/j.agwat.2017.04.016.

Vicca, S., Balzarolo, M., Filella, I., Granier, A., Herbst, M., Knohl, A., Longdoz, B., Mund, M., Nagy, Z., Pintér, K., Rambal, S., Verbesselt, J., Verger, A., Zeileis, A., Zhang, C., Peñuelas, J., 2016. Remotely-sensed detection of effects of extreme droughts on gross primary production. Sci. Rep. 6 (1), 28269. https://doi.org/10.1038/srep28269.

Vicente-Serrano, S.M., 2007. Evaluating the impact of drought using remote sensing in a mediterranean, semi-arid region. Nat. Hazards 40 (1), 173–208. https://doi.org/10.1007/s11069-006-0009-7.

Wan, Z., Hook, S., & Hulley, G. (2021a). MODIS/Aqua land surface temperature/emissivity daily L3 global 1km SIN Grid V061 doi:10.5067/MODIS/MYD11A1.061.

Wan, Z., Hook, S., & Hulley, G. (2021b). MODIS/Terra land surface temperature/emissivity daily L3 global 1km SIN grid V061. doi:10.5067/MODIS/MOD11A1.061.

Wehr, R., Saleska, S.R., 2021. Calculating canopy stomatal conductance from eddy covariance measurements, in light of the energy budget closure problem. Biogeosciences 18 (1), 13–24. https://doi.org/10.5194/bg-18-13-2021.

Whitehead, D., 1998. Regulation of stomatal conductance and transpiration in forest canopies. Tree Physiol. 18 (8-9), 633–644. https://doi.org/10.1093/treephys/18.8-9.633.

Wolf, S., Eugster, W., Ammann, C., Häni, M., Zielis, S., Hiller, R., Stieger, J., Imer, D., Merbold, L., Buchmann, N., 2013. Contrasting response of grassland versus forest carbon and water fluxes to spring drought in Switzerland. Environ. Res. Lett. 8 (3), 035007 https://doi.org/10.1088/1748-9326/8/3/035007.

Xu, H.J., Wang, X.P., Zhao, C.Y., Yang, X.M, 2018. Diverse responses of vegetation growth to meteorological drought across climate zones and land biomes in northern China from 1981 to 2014. Agric. For. Meteorol. 262, 1–13. https://doi.org/10.1016/j.agrformet.2018.06.027.

Yebra, M., Van Dijk, A., Leuning, R., Huete, A., Guerschman, J.P., 2013. Evaluation of optical remote sensing to estimate actual evapotranspiration and canopy conductance. Remote Sens. Environ. 129, 250–261. https://doi.org/10.1016/j.rse.2012.11.004.

Zha, T., Barr, A.G., van der Kamp, G., Black, T.A., McCaughey, J.H., Flanagan, L.B., 2010. Interannual variation of evapotranspiration from forest and grassland ecosystems in western canada in relation to drought. Agric. For. Meteorol. 150 (11), 1476–1484. https://doi.org/10.1016/j.agrformet.2010.08.003.

Zhang, Y., Xiao, X., Zhou, S., Ciais, P., McCarthy, H., Luo, Y., 2016. Canopy and physiological controls of GPP during drought and heat wave. Geophys. Res. Lett. 43 (7), 3325–3333. https://doi.org/10.1002/2016GL068501.